Slow spin dynamics and quantum tunneling of magnetization in the dipolar antiferromagnet $DyScO_3$

N. D. Andriushin,[1,*] S. E. Nikitin,[2] G. Ehlers,[3] and A. Podlesnyak[4]

[1]*Institut für Festkörper- und Materialphysik, Technische Universität Dresden, D-01069 Dresden, Germany*
[2]*Quantum Criticality and Dynamics Group, Paul Scherrer Institute (PSI), CH-5232 Villigen, Switzerland*
[3]*Neutron Technologies Division, Oak Ridge National Laboratory, Oak Ridge, Tennessee 37831, USA*
[4]*Neutron Scattering Division, Oak Ridge National Laboratory, Oak Ridge, Tennessee 37831, USA*

(Received 27 April 2022; revised 20 July 2022; accepted 22 August 2022; published 23 September 2022)

We present a comprehensive study of static and dynamic magnetic properties in the Ising-like dipolar antiferromagnet (AFM) $DyScO_3$ by means of DC and AC magnetization measurements supported by classical Monte Carlo calculations. Our AC-susceptibility data show that the magnetic dynamics exhibit a clear crossover from an Arrhenius-like regime to quantum tunneling of magnetization (QTM) at $T^* = 10$ K. Below $T_N = 3.2$ K, $DyScO_3$ orders in an antiferromagnetic *GxAy*-type magnetic structure and the magnetization dynamics slow down to the minute timescale. The low-temperature magnetization curves exhibit complex hysteretic behavior, which depends strongly on the magnetic field sweep rate. We demonstrate that the low-field anomalies on the magnetization curve are related to the metamagnetic transition, while the hysteresis at higher fields is induced by a strong magnetocaloric effect. Our theoretical calculations, which take into account dipolar interaction between Dy^{3+} moments, reproduce essential features of the magnetic behavior of $DyScO_3$. We demonstrate that $DyScO_3$ represents a rare example of an inorganic compound, which exhibits QTM at a single-ion level and magnetic order due to classical dipolar interaction.

DOI: 10.1103/PhysRevB.106.104427

I. INTRODUCTION

Timescale of spin dynamics—the time required to flip a single spin—in conventional magnetic materials is of the order of femto- to picosecond [1–3]. Anomalous slowing down by multiple orders of magnitude down to the millisecond range is known take place in some single-molecule magnets and is induced by strong uniaxial anisotropy [4–6]. In that case, the strong crystalline electric field (CEF) splits the ground-state multiplet **J** of a magnetic ion and creates a doublet ground state, which consists of two states with maximal projection of angular momentum, pointing in the opposite directions, $|\psi_{\pm}^0\rangle = |\pm J\rangle$. Thus the direct transition between $|\psi_{+}^0\rangle$ and $|\psi_{-}^0\rangle$ states requires a change of the total momentum ΔJ by more than one, and thus is forbidden by selection rules of many conventional single-(quasi)particle emission/absorption processes. Therefore the matrix element for this transition is low, see Fig. 1(c).

In this case, there are two possible ways to change the spin momentum: (i) via an activation process to the excited doublet with wave functions $|\psi_{\pm}^1\rangle = |\pm J \mp 1\rangle$; or (ii) as a direct transition between $|\psi_{+}^0\rangle$ and $|\psi_{-}^0\rangle$ via the quantum tunneling of magnetization (QTM) process [4]. The first mechanism dominates in the temperature range $T \gtrsim \Delta_{CEF}/k_B$ (Δ_{CEF} is the energy gap to the excited doublet and k_B is the Boltzmann constant), but it becomes ineffective at lower temperature where the QTM dominates the magnetic relaxation.

QTM is a well-known process in single-molecule magnets, however, to the best of our knowledge, among inorganic crystals there are only few well-documented examples including $Dy_2Ti_2O_7$ [7–12] and $Ca_3Co_2O_6$ [13,14]. In both cases, the strong CEF produces large uniaxial anisotropy, which freezes magnetic moments below a crossover temperature $T^* \approx 13$ and ≈ 9 K, for $Dy_2Ti_2O_7$ and $Ca_3Co_2O_6$, respectively. However, in addition to the QTM both materials also show complex collective magnetic behavior, classical spin-ice physics in case of $Dy_2Ti_2O_7$ and a frustrated spin-chain behavior in $Ca_3Co_2O_6$, which obscure the QTM physics. Another prominent example is a dipolar ferromagnet $LiHoF_4$ and its diluted modifications $LiHo_xY_{1-x}F_4$ [15–18], where electronic and nuclear spins of Ho^{3+} ions are coupled because of large hyperfine interaction, which produces complex slow dynamics at low temperatures.

In this work, we focus on a classical Ising-like dipolar AFM $DyScO_3$. This material crystallizes into a distorted perovskite structure with the *Pbnm* space group [Fig. 1(a)]. Because of octahedral distortion, Dy^{3+} ions occupy a low-symmetry position with only one symmetry element—the mirror plane perpendicular to the *c* axis. $DyScO_3$ is commonly used as a substrate for thin films growth, because of good mechanical properties and lattice match with perovskite superconductors [19–21]. Another active field or research is related to the sister compound, $DyFeO_3$, which displays multiferroic properties below the magnetic ordering temperature of Dy moments [22]. Until recently, the Dy^{3+} moments were thought to order into a commensurate AFM structure [23–25] and exchange striction mechanism involving both Fe and Dy subsystems was proposed to explain the

*Corresponding author: Nikita.Andriushin@tu-dresden.de

 ©2022 American Physical Society

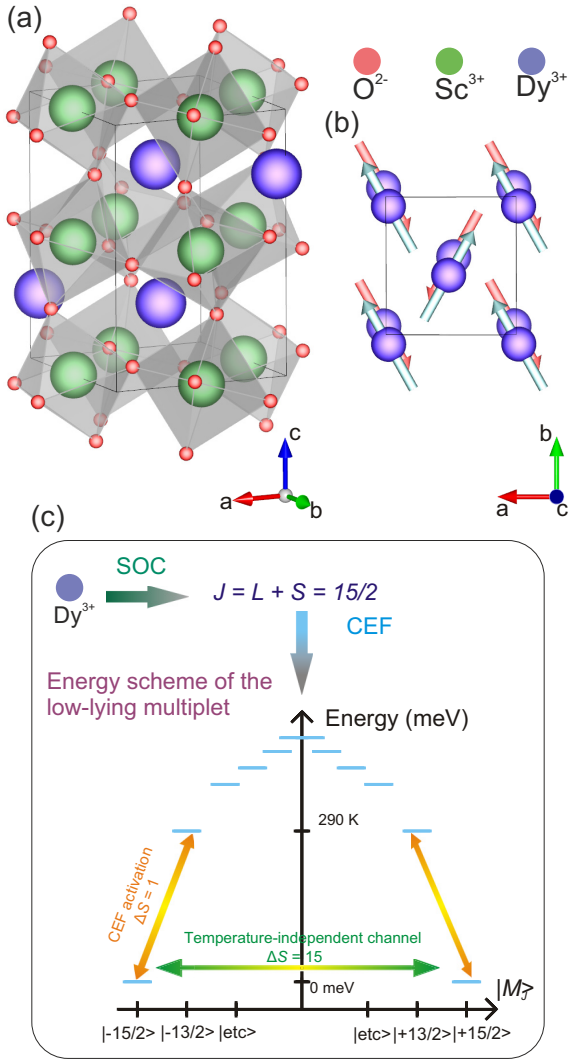

FIG. 1. Crystal (a) and magnetic (b) structure of $DyScO_3$. Red, green, and violet balls represent O^{2-}, Sc^{3+}, and Dy^{3+} ions, respectively. Red and light blue arrows represent arrangement of Dy moments at two neighbor layers for GxAy spin configuration [28]. (c) Sketch of the energy diagram of $\mathbf{J} = 15/2$ multiplet of Dy^{3+} in $DyScO_3$, shown in $|M_J\rangle$-E coordinates. Spin-orbit coupling (SOC) produces the $\mathbf{J} = 15/2$ multiplet, which is split into 8 doublets by CEF. The ground state doublet consists of $|\pm 15/2\rangle$ wave functions, following by excited $|\pm 13/2\rangle$, $|\pm 11/2\rangle$, etc. While the temperature dependence of the spin excitation associated with $|\pm 15/2\rangle \rightarrow |\pm 13/2\rangle$ transition follows Arrhenius law, the direct transition between $|\pm 15/2\rangle$ states is the temperature-independent QTM process.

multiferroic properties. However, very recently a high-resolution neutron diffraction study reported incommensurate elliptical spiral or spin density wave (SDW) order of Dy moments with $\mathbf{k} = (0\,0\,1 \pm \delta)$. Such an incommensurate magnetic structure could potentially have an impact on the dielectric response of $DyFeO_3$ due to lowering of the symmetry [26,27].

$DyScO_3$ is reported to exhibit noncollinear AFM ordering below $T_N = 3.2$ K with the propagation wave vector $\mathbf{k} = (0\,0\,1)$ (GxAy configuration) as shown schematically in Fig. 1(b) [28]. Magnetization and neutron diffraction measurements show that Dy have strong uniaxial anisotropy at low temperature and the easy axis lies in the *ab* plane, with a $\pm 28^\circ$ angle to the [010] direction [28–30]. Inelastic neutron scattering (INS) measurements show that the ground state doublet is well-isolated from the first excited doublet located at 290 K. Point-charge model calculations supported by magnetization measurements show that the wave function of the ground state doublet consists of almost pure $|\pm 15/2\rangle$ states, making $DyScO_3$ a prospective material to search for the QTM effect.

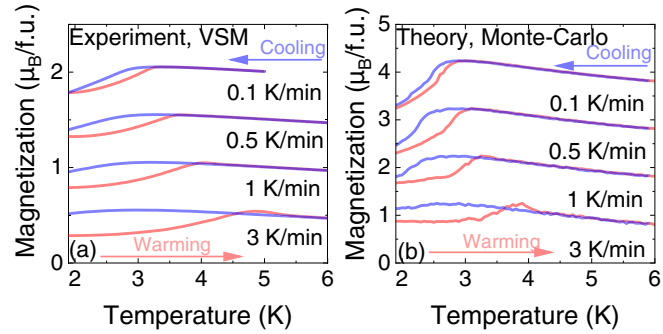

FIG. 2. Temperature dependencies of the magnetization of $DyScO_3$ measured using VSM at $B = 0.1$ T (a) and calculated by Monte Carlo (b) with different temperature sweep rates as described in Sec. II C. Red and blue lines represent data collected on warming and cooling, respectively. Data are in (a) and (b) are shifted respectively by $+0.5\ \mu_B$/f.u. and $+1\ \mu_B$/f.u. vertically for clarity.

In this work, we performed a comprehensive study of the low-temperature magnetic behavior in $DyScO_3$. We confirmed that Dy moments orders antiferromagnetically below $T_N = 3.1$ K via specific heat measurements. Our neutron diffraction data indicate that the ordering wavevector of $DyScO_3$ is—within the resolution of $\approx$0.01 r.l.u.—commensurate, which is a difference to $DyFeO_3$. We observed a clear peak in imaginary part of dynamical spin susceptibility χ''. It exhibits a crossover between an Arrhenius-like regime at high temperatures and a temperature-independent regime below $\lesssim$10 K, which is a fingerprint of QTM behavior. The $M(B)$ curves taken below T_N demonstrate complex hysteretic behavior. By using classical Monte Carlo simulations with dipolar interactions we reproduced essential features of magnetic behavior of $DyScO_3$: (i) the type of magnetic ordering and the ordering temperature T_N; (ii) temperature dependencies of the magnetic specific heat and magnetization; (iii) behavior of magnetic correlation length above the T_N; and (iv) kink and a broad magnetic hysteresis on the $M(B)$ curves. Our results demonstrate that the low-temperature behavior of $DyScO_3$ is described by a combination of CEF-induced QTM, dipolar intersite interaction and the strong magnetocaloric effect.

II. RESULTS AND ANALYSIS

A. Slow dynamics at low-field regime

We start the presentation of our results with the magnetization data collected as a function of temperature with different sweep rates as shown in Fig. 2(a). Note that the magnetic field was applied along the easy direction, which we

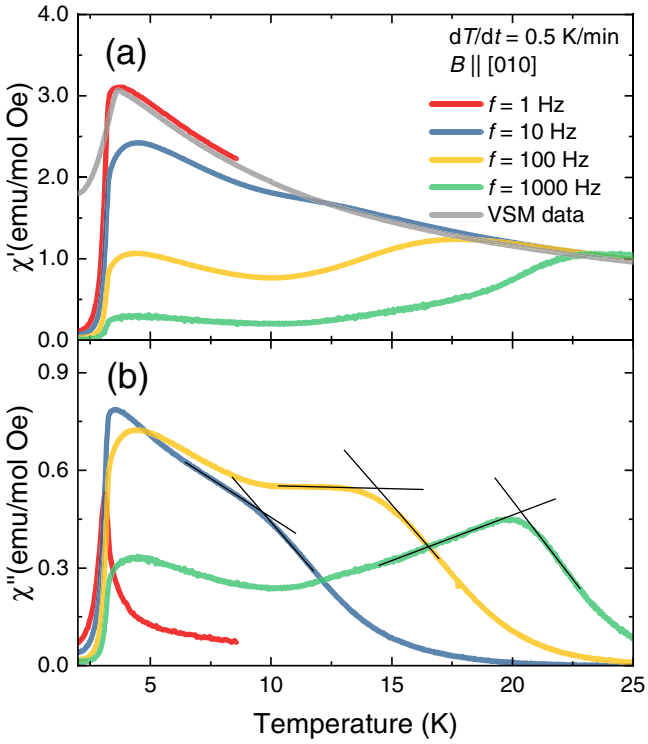

FIG. 3. Temperature dependence of real (a) and imaginary (b) parts of the complex longitudinal AC susceptibility of $DyScO_3$ measured with 5 Oe drive field for $f = 1, 10, 100$ Hz and 2.5 Oe for 1000 Hz applied along [010] at zero DC field. The static spin susceptibility M/B measured at $B = 0.1$ T using VSM is shown in (a). Crossed black lines in (b) illustrate how the crossover temperatures was determined for $f = 10,\ 100$, and 1000 Hz curves.

define as the direction, for which the bulk magnetization is maximal, $B \parallel [010]$ [28], in all measurements and calculations. All curves collected upon warming up show a clear cusp anomaly associated with AFM ordering. Noticeably, the position of the cusp shifts with the sweep rate dT/dt. One can also see that the field-cooling (FC) curves differ considerably from those collected upon warming up (i) the cusp associated with the AFM transition becomes less well-defined and is almost gone for $dT/dt \geqslant 1$ K/min and (ii) the FC and warming up curves show considerable hysteresis below T_N.

These results indicate the presence of a considerable magnetization relaxation at low temperatures, that takes place on a timescale of minutes, which is unexpected for a conventional antiferromagnet. In order to get further insight to the slow dynamics of $DyScO_3$, we have measured temperature and frequency dependencies of the complex magnetic susceptibility $\chi(f, T)$ and the results are shown in Figs. 3 and 4. Figure 3(a) displays the temperature dependence of the real part of the AC susceptibility, $\chi'(T)$, measured at different frequencies along with the static spin susceptibility, M/B, measured with VSM. The curves collected at $f = 1$ Hz and at static regime agree well above T_N, and display a single peak at the transition temperature. The qualitative behavior changes when the frequency is increased. The low-temperature susceptibility measured at $f \geqslant 10$ Hz is reduced, but returns to M/B above a frequency-dependent crossover temperature. The high-temperature tails of all curves follow the same Curie-Weiss law.

The $\chi''(T)$ curve measured at 1 Hz shows a strong divergence at T_N, as expected for an AFM system. With increasing frequency the shape of the peak at the ordering temperature changes significantly and becomes similar to the one observed in $\chi'(T)$. Moreover, we observed the second peaklike anomaly, whose positions shifts with frequency. We quantified the positions of the second anomaly using the inflection point, as shown for $f = 10,\ 100$, and 1000 Hz curves in Fig. 3(b). The obtained frequency-dependent timescales characterize the magnetization dynamics and are plotted with green circles in Fig. 6.

To reveal the frequency dependence of the spin susceptibility in $DyScO_3$ we measured $\chi'(f)$ and $\chi''(f)$ at multiple temperatures, and several representative curves are

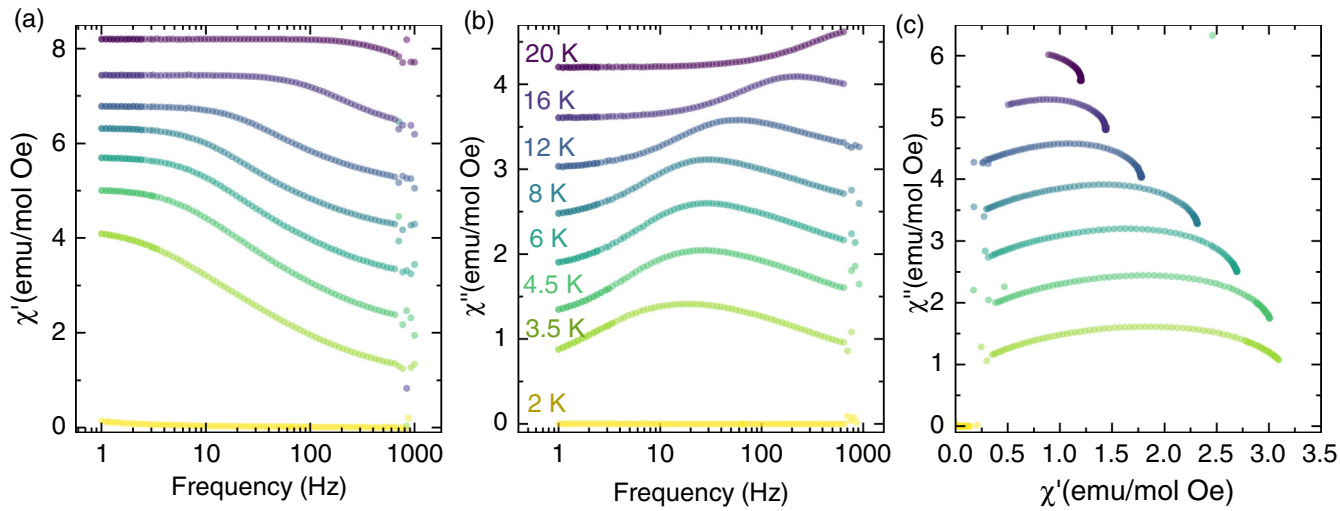

FIG. 4. Frequency dependence of the AC susceptibility measured at multiple temperatures between 2 and 20 K. (a) and (b) show the real $[\chi'(f)]$ and imaginary $[\chi''(f)]$ parts of the AC susceptibility, respectively. (c) shows the Cole-Cole plot $\chi''(\chi')$. All data are shown with a constant vertical offset for clarity.

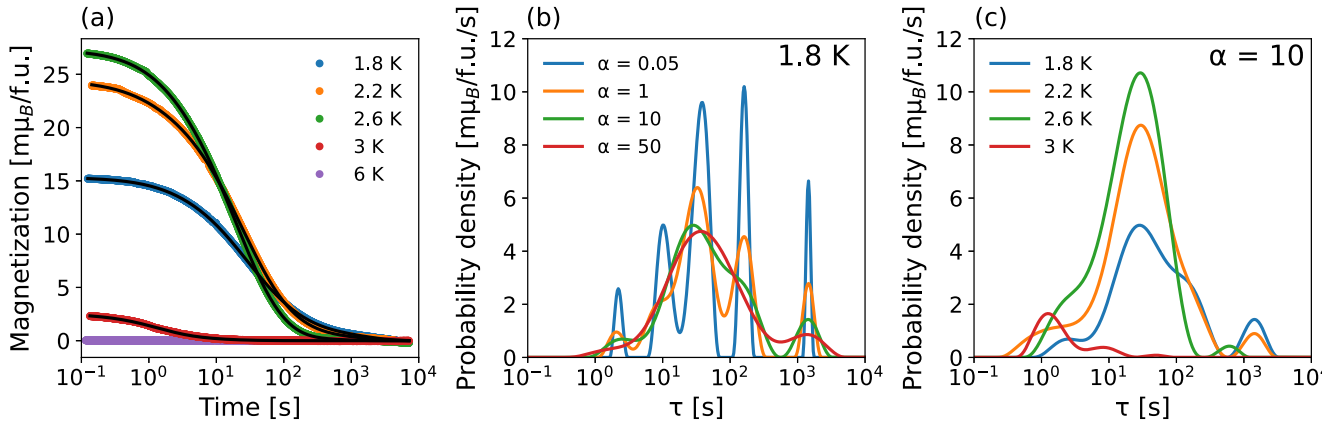

FIG. 5. Time dependence of magnetization taken after switching off 0.01 T magnetic field. Color dots and black lines in panel (a) show experimental data and relaxation calculated with ILT. (b) Relaxation time distribution function calculated for $T = 1.8$ K curve using different regularization parameter α as detailed in legend. (c) Relaxation time distribution function calculated for $\alpha = 10$ and different temperatures.

shown in Fig. 4. The $\chi'(f)$ demonstrates a plateau at low frequencies and a gradual decrease above temperature-dependent crossover frequency. The $\chi''(f)$ curves display a strong broad peak at $T \geqslant 3$ K. The position of the peak shifts down with decreasing temperature, however between $T = 10$ and 4 K $\chi''(f)$ remains almost unchanged. When cooling below T_N the peak height decreases and shifts towards lower frequencies, which could not be followed further with our AC setup. Figure 4(c) shows Cole-Cole plots $\chi''(\chi')$ at different temperatures. For a system with a single relaxation channel (or symmetrical distribution of the relaxation channels), the curves should follow a semicircular trajectory. However, the curves measured with $DyScO_3$ are asymmetric, indicating a more complex distribution of the relaxation times [31–33].

To characterize the timescale of the magnetization dynamics below T_N we used a VSM magnetometer and measured magnetization relaxation after switching off 100 Oe DC magnetic field. Further discussion of the protocol details is given in Sec. A of Appendix. The relaxation curves collected at several selected temperatures above and below T_N are shown in Figs. 5(a) and 5(b). The most striking feature is that the magnetization displays slow exponential-like relaxation at $T \leqslant 2.6$ K. At $T = 3$ K (close to T_N), the relaxation takes place considerably faster and the relaxing moment decreases, while at 6 K, two time T_N, we did not observe any relaxation within the resolution of our setup, which clearly shows that the dynamics on minute time scale is associated with magnetic ordering.

Conventionally, the relaxation process $M(t)$ can be described with an exponential function with a single characteristic relaxation time τ [Eq. (1) with $\beta = 1$]. In systems which have a distribution of relaxation times, for example, due to an overdamping or disorder, the simple exponent model may fail [34]. A commonly used, more advanced, approach to a relaxation description is the time-stretched exponent:

$$M(t) = M_0 e^{-(t/\tau)^{\beta}}. \tag{1}$$

Here, the new parameter $\beta \in [0, 1]$, introduces a stretching of exponential decay. For this function the characteristic relaxation time is not a single value but a continuous distribution of relaxation times with a maximum near the τ parameter and the width given by β. However, we were not able to obtain good fit of our experimental data taken at $T < 3$ K using a Eq. (1) meaning that the distribution of relaxation times in $DyScO_3$ cannot be described in this way.

By choosing a fitting model for relaxation data, we always assume a certain distribution of relaxation time: a delta function for a single exponent, a set of delta functions in case if we use a sum of several exponent relaxations or a continuous peak of certain width in case of stretched exponent. All these models can be generalized using the relaxation-time distribution function as follows:

$$M(t) = \int_0^{\infty} P(\tau) e^{-(t/\tau)} d\tau. \tag{2}$$

Equation (2) describes a Laplace transform of a relaxation time distribution $P(\tau)$, the values of which give a probability that system will relax with a time constant τ. In an experiment, we measure $M(t)$ and afterwards extract information about a relaxation time distribution $P(\tau)$ by fitting with a phenomenological function. Direct calculation of $P(\tau)$ from the experimental data is difficult, because the inverse Laplace transform (ILT) is a mathematically ill-posed problem and it may have far more than one solution. However, there are some algorithms which make use of the fact that the relaxation time distribution only has physical meaning if τ is a non-negative real number. We performed the ILT of our magnetization data using the regularized non-negative least-square method, for details of the method see Appendix A.

The ILT algorithm we applied to the analysis of our data requires a single regularization parameter α as input. The parameter α controls how broad in τ the distribution function $P(\tau)$ is. Therefore, as the first step, we selected α by calculating the ILT for 1.8 K data using several different regularization parameters α. The relaxation time distribution function for four representative α are shown in Fig. 5(c). For small $\alpha = 0.05$ and 1, the relaxation times distribution shows a complex profile with multiple peaks, some of which are located very close to each other. For $\alpha = 10$, the distribution function becomes simpler and exhibits two peaks: a broad peak at 30 s and the second peak at $\tau \approx 1500$ s, which is 5–10 times

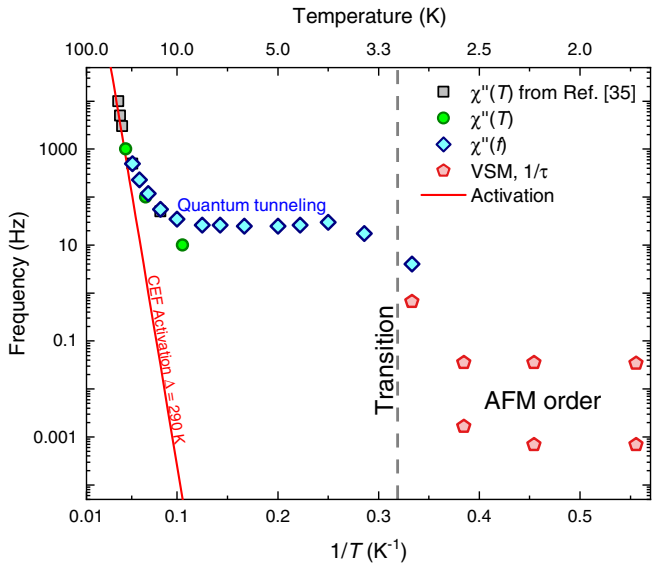

FIG. 6. Arrhenius plot $\log(f)(1/T)$, reconstructed from our results along with data from Ref. [35]. The grey dotted line shows the transition temperature T_N. The blue and green points show the peak positions extracted from the frequency and temperature dependencies of imaginary part of AC susceptibility χ'', and the black squares show the high-frequency data from Ref. [35]. Red solid line shows the calculated CEF activation curve with experimentally determined $\Delta = 290$ K. Red points show inverse relaxation constants $1/\tau$ extracted as positions of probability density maximum calculated with the ILT.

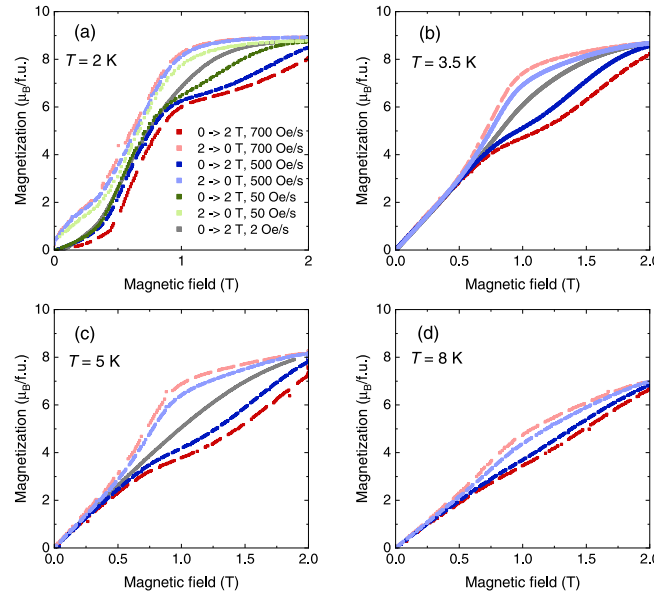

FIG. 7. Magnetization curves $M(B)$ measured at several temperatures as indicated at each panel. The curves were measured with different sweep field rates as shown in legend.

weaker than the primary fast relaxation. Both observed peaks are broad, which correspond to finite distribution width of the relaxation times [$\beta < 1$ in Eq. (1)]. With further increase of α the distribution function does not change qualitatively and two peaks in τ remain its primary feature. We note that ILT convolutions with different α provide similar quality of the data description and therefore we cannot uniquely identify, which time distribution is realized in $DyScO_3$. However, having no physical justification to assume that the relaxation dynamics in $DyScO_3$ is associated with multiple narrow-in-τ relaxation channels and taking into account that for $\alpha > 10$ the $P(\tau)$ function shows only weak quantitative changes we have fixed empirically $\alpha = 10$ throughout our analysis. In Fig. 5(d), relaxation times distributions obtained with the ILT calculation are shown for $T = 1.8$–3 K. At $T = 3$ K, the weak slow peak becomes nonvisible in the ILT profile. To check quality of the ILT we calculated Laplace transform of it and compare the result with the original $M(t)$ data as shown by solid black lines in Fig. 5(a) and one can see very good agreement. From the ILT calculations, we conclude that $DyScO_3$ has single relaxation channel at $T = 3$ K ($\tau = 2$ s) and two channels at $\tau \approx 28$ and $\approx$1500 s below 3 K. Note that we quantify τ as position of the maximum of the peaks in $P(\tau)$ curves.

The temperature dependence of observed relaxation times extracted from AC susceptibility and magnetization relaxation measurements is summarized in Fig. 6. Informed by our own INS measurements [28], we highlight three different regimes: (i) Arrhenius regime at high-temperature, $T > 10$ K; (ii) temperature-independent relaxation between 10 K and T_N; and (iii) slow relaxation in the AFM phase. The temperature dependent AC susceptibility in $DyScO_3$ was also studied in Ref. [35], where the authors observed peaklike anomalies in $\chi''(T)$ curves, which shifted with frequency. The authors associated this peak with an Arrhenius-like relaxation process, taking the population of the CEF level into account, and extracted $\Delta/k_B = 229$ K. Our own later INS measurements indicated that the first CEF level is located at higher energy, $\Delta/k_B = 290$ K [28]. The calculated curve for a 290 K gap is shown in Fig. 6 by a red line, and one can see good agreement with experimental points at high temperature and a clear crossover between regimes (i) and (ii).

The behavior seen in $DyScO_3$ strongly resembles the slowing down of the spin dynamics in a classical spin-ice compound $Dy_2Ti_2O_7$, which also shows three regimes at different temperatures: (i) Arrhenius relaxation at $T > 15$ K; (ii) plateau at $1.5 < T < 15$ K; and (iii) another Arrhenius regime below 1.5 K due to development of the spin-ice regime [7,9,10]. The difference in the low-temperature regime (iii) is a consequence of the different ground states, AFM in $DyScO_3$ vs. spin-ice in $Dy_2Ti_2O_7$.

B. Field-induced anomalies

We next proceed with a description of the field-induced physics in $DyScO_3$. Authors of Ref. [28] reported magnetization curves measured at $T = 2$ K along three crystallographic directions. Interestingly, the curves measured along [010] and [100] axes show two consecutive hystereses at low field and just below the saturation. These features were interpreted as two field-induced first-order phase transitions. Motivated by those observations we measured the magnetization of $DyScO_3$ at several temperatures with magnetic field applied along the [010] axis. Figure 7 shows magnetization curves collected at several temperatures below and above T_N. One can see that

at $T = 2$ K magnetization curves measured with high sweep rates (50, 500, and 700 Oe/s) show considerable hysteresis over the whole field range. However, we can clearly highlight two distinct transitions: the first kink at $B \approx 0.4$ T and the second anomaly at $B \approx 1$ T. Noticeably, when the sweep rate decreases, only the low-field features remains visible, while magnetization at higher fields shows simple Brillouin-like behavior. Figures 7(b)–7(d) demonstrate magnetization collected above T_N and one can see that the magnetization is perfectly linear at the low-field regime in agreement for the expectation for a paramagnet. However, the clear kink as well as the hysteresis at 0.7–2 T are clearly seen for high field-sweep rates, while the low-sweep curves show simple Brillouin-like behavior.

Based on these data we can associate the first transition with the field-induced destruction of the AFM order, while the high-field hysteresis is associated with single-ion physics, because it persists to temperatures up to ~8 K, which is much larger than the characteristic energy scale of magnetic interactions in $DyScO_3$. We associate this effect with the strong magnetocaloric effect (MCE) in $DyScO_3$ [36] and in the next section we show that Monte Carlo simulations, which take into account the MCE, are capable to reproduce this effect.

C. Monte Carlo simulations

As discussed above, $DyScO_3$ shows strong Ising-like single-ion anisotropy of magnetic moments, meaning that Dy moments can be pointed up or down along the CEF-dictated easy magnetization direction at each site. In addition, a previous report associated magnetic order with the dipole-dipole interactions between Dy moments [28]. The standard approach to describe physical properties of an Ising system on a 3D lattice is by Monte Carlo modeling and here we make use of the metropolis algorithm to describe magnetic behavior of $DyScO_3$ [37]. We considered a $10\times10\times10\times4$ cluster of Ising spins, which are coupled by dipole-dipole interaction and are in thermal contact with a reservoir at temperature T_{res}. Most parameters of our model, such as interatomic distances, the field and temperature dependence of the thermal conductivity (approximated from the data measured on isostructural $DyAlO_3$), the magnetic moment of Dy^{3+} and the direction of easy axis were fixed from the experimental data [28,38]. The only free parameter is the coefficient which converts the number of Monte Carlo steps to the experimental time, which we fixed by comparison of calculated and experimental $\chi''(f)$ curves and the absolute value of the thermal conductivity. See Appendix B for details.

We start the presentation of our calculations with the low-temperature magnetic structure. First, our MC calculations show that the *GxAy* is the ground state of $DyScO_3$ and has the lowest energy among the four possible $\mathbf{k} = 0$ magnetic configurations in $DyScO_3$, in agreement with previous estimates for smaller clusters [28,36]. As the next step we calculated the static magnetic structure factor, $S(\mathbf{Q})$, and found that the AFM order manifests itself with a strong magnetic Bragg peak at $\mathbf{Q} = (001)$. We plot the calculated temperature dependence of (001) peak in Fig. 8 along with the experimental measurements of the ordered moment [28]. Fitting of calculated data near the critical temperature was performed using the

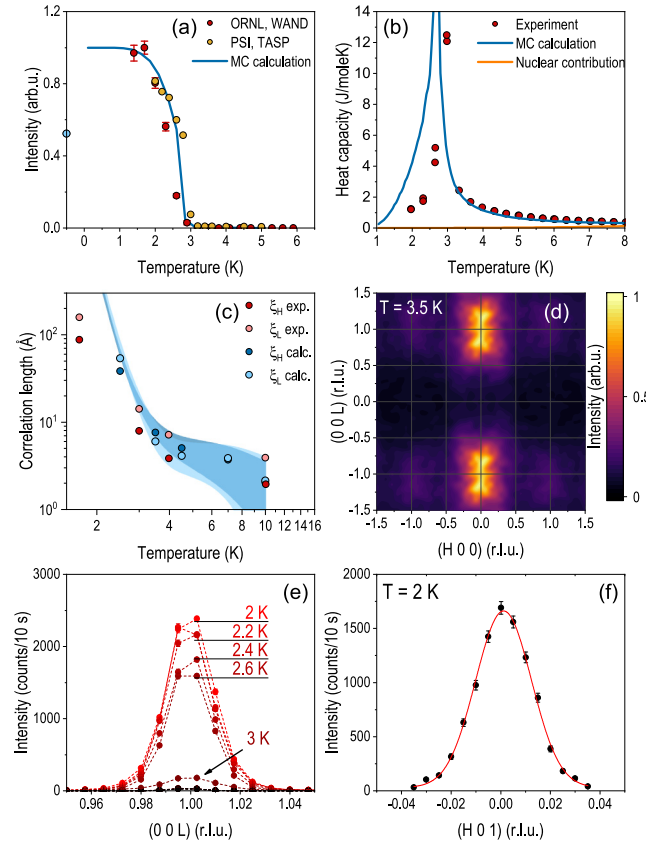

FIG. 8. AFM ordering at zero field. (a) Temperature dependence of (001) Bragg peak. Red dots represent experimental data extracted from neutron powder diffraction [28]. Orange dots show data obtained by single-crystal neutron diffraction on TASP instrument. The solid line is the result of Monte Carlo calculations. (b) Calculated and measured low-temperature specific heat. The nuclear contribution was approximated by $C(T) = \beta T^3$ with $\beta = 0.23$ mJ mole^{-1} K^{-4} and added to the calculated curve. The nuclear contribution reaches 0.047 J mole^{-1} K^{-1} at $T = 6$ K and therefore is barely visible at this temperature scale. (c) Temperature dependence of the correlation length measured by neutron diffuse scattering (red and pink dots) [28] and calculated by Monte Carlo (blue and light blue dots). The filled area represents the estimated uncertainty of the calculation. (d) Simulated neutron diffraction pattern in the $(H0L)$ scattering plane calculated at $T_N < T = 3.5$ K showing anisotropic diffuse scattering around the primary AFM peak (001). (e) Neutron scattering intensity of (001) peak measured at multiple temperatures using TASP instrument. (f) Neutron scattering intensity of (001) peak at 2 K, measured along $(H00)$ direction.

following expression:

$$S = \begin{cases} 0, & \text{for } (T > T_c) \\ S_0\left(1 - \left(\frac{T}{T_c}\right)^{\beta}\right)^{\alpha}, & \text{for } (T \leqslant T_c) \end{cases}$$

and yielded the critical temperature $T_N = 2.853(1)$ K. The very good agreement with the experimentally determined $T_N = 3.11$ K indicates that the dipolar interaction is the primary magnetic interaction in $DyScO_3$. We have also modeled the magnetic diffuse scattering above the transition temperature. The representative diffuse pattern calculated at

$T = 3.5$ K is represented in Fig. 8(d), which was obtained from averaging a number of Monte Carlo runs. We extracted the temperature dependence of the correlation length [Fig. 8(c)] and compared it with experimental results measured at the CNCS instrument [28]. Clearly, the measured and the calculated curves show good agreement with $\xi_c > \xi_{ab}$ over all temperature range. The reason is the mutual arrangement of crystal axes and directions of Dy^{3+} moments: the nearest neighbor Dy moments along the c axis have strong antiferromagnetic interaction, while interaction between in-plane Dy moments is nearly canceled out for the $GxAy$ magnetic configuration [36]. To further characterize the magnetic transition we calculated the specific heat of $DyScO_3$ and show it along with the experimental curve in Fig. 8(b). Both curves show a sharp λ-like peak at T_N due to AFM transition with only weak shoulders above T_N, which indicates weak magnetic correlations in the paramagnetic state. The entropy change associated with anomaly in the specific heat is in agreement with the value expected for a Ising system: $R\ln(2S+1)$ for $S = 1/2$.

Note that very recently, an incommensurate AFM order of Dy moments with propagation wave vector $\mathbf{k} = (0\,0\,1 \pm \delta)$ was observed in the isostructural compound $DyFeO_3$. In order to verify that $DyScO_3$ shows simple commensurate order we performed high-resolution single crystal neutron diffraction measurements using TASP triple axis instrument at PSI and the scans at along h and l directions of reciprocal space around (0 0 1) peak are shown in Figs. 8(e) and 8(f). No splitting of the AFM peak observed within the resolution of ≈0.01 r.l.u. This result indicates that the zero-field magnetic order in $DyScO_3$ is commensurate in agreement with previous report [28] and our MC calculations, but in contrast to $DyFeO_3$. We further speculate that our results supports the hypothesis that the splitting of (0 0 1) peak in $DyFeO_3$ could be associated with interaction between Dy and Fe subsystems.

To reveal the origin of the bifurcation between the $M(T)$ curves shown in Fig. 2(a), we performed Monte Carlo simulations of the temperature dependences of magnetization [see Fig. 2(b)] with different sweep rates of the reservoir temperature, dT_{res}/dt. We found that the calculated magnetization curves are in qualitative agreement with experimental data. Specifically, the magnetization curve calculated for $dT/dt = 0.1$ K/min shows a clear cusp at T_N and a weak hysteresis below the transition. With increase sweep rate dT/dt the hysteresis becomes wider and the peak for warming up curves shifts towards higher temperatures in good qualitative agreement with the experiment. The reason for this behavior is the poor thermal stabilization due to both, weak thermal conductivity and slow thermalization during the temperature sweeps, because of which the actual temperature of the sample can differ considerably from T_{res}. This effect causes bifurcation between cooling and warming $M(T)$ curves and the sweep-rate dependence of the transition temperature.

As the next step we calculated the magnetic field dependence of the magnetization at three characteristic temperatures of the reservoir, $T_{res} = 1$, 2, and 3.5 K and the results are summarized in Fig. 9. We performed two versions of calculations, (i) isothermal magnetization with $T_{Sample} = T_{res}$ strictly maintained, and (ii) by taking into account the strong magnetocaloric effect [29], see details of calculations in

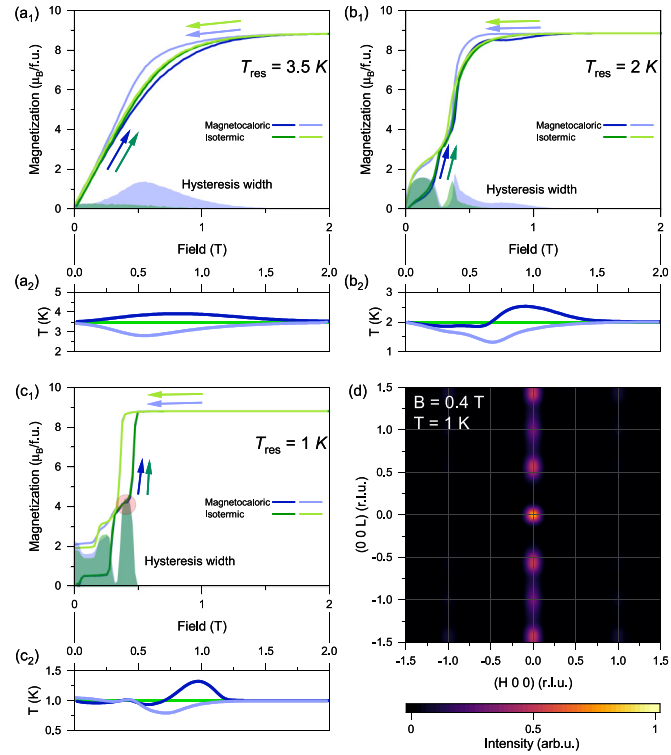

FIG. 9. [(a1)–(c1)] The magnetization curves calculated taking into account magnetocaloric effect at various temperatures of reservoir and corresponding system temperature dependence. The magnetization curves were calculated for external field ramped from zero to 2 T and backward, the shaded areas show width of the hysteresis curves $\Delta M(B) = M(B)\uparrow - M(B)\downarrow$. Additional panels (a2)–(c2) show temperature change during simulation, grey horizontal lines denote reservoir temperatures. Reservoir temperatures are indicated in each panel. The contour map (d) is the calculated magnetic structural factor for the incommensurate state around $B = 0.4$ T and $T = 1$ K [red circle at (c1)].

Appendix B. The field sweep rate for all curves in Fig. 9 was 0.5 T/min.

First of all, let us consider the magnetization curves calculated at $T = 3.5$ K above the ordering temperature, which are shown in Fig. 9(a1). The isothermal magnetization calculated at $T = 3.5$ K shows featureless Brillouin-like behavior in agreement with expectations for a paramagnet. Introduction of the magnetocaloric effect changes qualitative behavior of the magnetization curves and opens a broad hysteresis at $B \approx 0.4$–1.2 T, because of the field-induced change of T_{samp}, which is shown in Fig. 9(a2). Thus we conclude that the hysteresis at intermediate fields observed in our magnetization measurements for $dB/dt \geqslant 50$ Oe/s (Fig. 7) is caused by the magnetocaloric effect, which however plays a minor role when the field ramp rate is small compared to the thermalization time, meaning that $T_{samp} = T_{res}$.

Below the magnetic transition temperature the magnetization curve changes considerably. The curves calculated at $T_{res} = 2$ K demonstrate a metamagnetic transition and a broad hysteresis at low fields, $B < 0.3$ T, which behaves similarly for both, the isothermal and nonisothermal curves [Fig. 9(b1)]. Above the metamagnetic transition the isothermal curves merge and show the featureless Brillouin-like behavior, while

a narrow hysteresis emerges at $B = 0.5$–1 T for the curves calculated with magnetocaloric effect. We note that the exact shape of the calculated curve depends considerably on the thermal conductivity of $DyScO_3$, which depends on both magnetic field and temperature, $\lambda(B, T)$. This quantity was not measured in the low-temperature regime, $T < 10$ K and in our calculations we make use of the data measured in the paramagnetic phase on the isostructural $DyAlO_3$ [38], which we approximate down to the temperature range of interest (see Appendix B for details). This procedure does not provide quantitatively precise values for the thermal conductivity, especially below T_N where thermal conductivity can exhibit strong anomalies near the critical field [39–41]. Therefore the exact shape of calculated and observed magnetization curves does not match quantitatively. However, our calculations allow us to associate the high-field hysteresis with the magnetocaloric effect, while the low-field anomalies, including the metamagnetic transition and the hysteresis of magnetization, are associated with collective behavior.

Figure 9(c1) shows magnetization calculated at $T_{res} = 1$ K and one can see that isothermal and nonisothermal curves coincide over all field scales, meaning that the magnetocaloric effect has a minor influence on the magnetization curve at this temperature. Moreover, the curves calculated for $B = 0 \rightarrow 2$ T demonstrate a narrow $M_s/2$ plateau at $B = 0.4$ T. In a system with Ising-like anisotropy, the magnetic moments can point parallel or antiparallel to the easy-axis direction, therefore below the ordering temperature, one can expect to see the formation of SDW-like incommensurate phases at the intermediate magnetic fields [42,43]. Figure 9(d) shows the calculated static spin structure factor at $T = 1$ K and $B = 0.4$ T, which corresponds to the plateau field range. One can see clearly formation of the incommensurate peaks at $\mathbf{q} = (0\,0\,0.55)$, which can be associated with the formation of $\uparrow\uparrow\uparrow\downarrow$ type of order along the c axis. Two other reflections correspond to the primary magnetic reflection of the zero-field AFM phase, $\mathbf{q} = (0\,0\,1)$ and ferromagnetic $\mathbf{q} = (0\,0\,0)$ peak. We note that a similar field-induced incommensurate magnetic order with $\mathbf{k} = (0\,0\,1 \pm \delta)$ was observed previously in the isostructural material $YbAlO_3$ [44,45]. Moreover, very recently an incommensurate order (SDW or eliptical spiral) with $\mathbf{k} = (0\,0\,1 \pm \delta)$ was reported in another isostructural compound $DyFeO_3$ [26,27], where it could be related with interaction between Fe and Dy magnetic subsystems. Low-temperature in-field neutron diffraction measurements would be required to verify the presence of the incommensurate field-induced magnetic phases in $DyScO_3$.

III. DISCUSSION AND CONCLUSION

We demonstrate that $DyScO_3$ exhibits slow dynamics of magnetization below $T^* = 10$ K, which is caused by strong CEF-induced uniaxial anisotropy of Dy^{3+} moments. We note that similar behavior was observed previously in multiple organic-based magnetic molecules [4–6], while such a behavior in inorganic materials remains relatively rare. Several representative examples are $Dy_2Ti_2O_7$ and $Ca_3Co_2O_6$. However, in addition to the QTM, both aforementioned materials display complex magnetic behavior due to frustration of magnetic interactions. The presence of the competing interactions makes it difficult to disentangle the effects of QTM and magnetic frustration on spin freezing in these systems, contrary to the case of $DyScO_3$. We have characterized the low-temperature spin dynamics of $DyScO_3$ using AC susceptibility and magnetization relaxation measurements and have observed three regimes: Arrhenius-like behavior at $T > T^*$, a plateau between T^* and T_N, and slow relaxation of magnetization below T_N. Thus $DyScO_3$ represents a so-far unique example of a classical dipolar AFM, which combines a classical magnetically ordered ground state with QTM.

Our Monte Carlo simulations appear to capture the essential physics of $DyScO_3$, including the magnetic ground state, the temperature of the AFM transition, slow dynamics of magnetization at low temperatures and bifurcation between $M(T)$ curves collected upon cooling and warming. In addition, by taking into account the magnetocaloric effect we were able to describe the magnetization curves and demonstrate that the hysteresis in the paramagnetic phase is caused by considerable field-induced change of the sample temperature during the measurements. Our simulations also predict the formation of an incommensurate spin-density wave magnetic phase at low temperatures and intermediate magnetic fields, similar to that observed in $YbAlO_3$ [44,45], whose existence in $DyScO_3$ awaits experimental verification with elastic neutron scattering measurements.

We note that although our model captures the main features of magnetic behavior in $DyScO_3$ there are minor quantitative disagreements such as the exact shape of the hysteresis curves shown in Figs. 7(a)–7(c), which could probably be improved by including in the model exact results for the field- and temperature-dependence of thermal conductivity. In addition, the $\chi''(\chi')$ curve has an asymmetric shape indicating a complex distribution of the relaxation times, while our model implies a single relaxation channel for simplicity.

To conclude, we have applied AC susceptibility and DC magnetization measurements, supported by specific heat, neutron diffuse scattering and Monte Carlo calculations to characterize spin dynamics in $DyScO_3$. Our results indicate that $DyScO_3$ represents a rare combination of single-ion QTM behavior with classical dipolar interactions and stimulate further search of rare-earth based condensed matter systems with QTM.

ACKNOWLEDGMENTS

We thank O. Stockert and A. S. Sukhanov for stimulating discussions and A. Turrini for help with neutron diffraction measurements. S.E.N. acknowledges financial support from the European Union Horizon 2020 research and innovation program under Marie Skłodowska-Curie Grant No. 884104. The work of N.D.A. was supported by the German Research Foundation (DFG) through Grant No. PE 3318/3-1. This research used resources at the Spallation Neutron Source, a DOE Office of Science User Facility operated by the Oak Ridge National Laboratory. This work is based on experiments performed at the Swiss spallation neutron source SINQ, Paul Scherrer Institute, Villigen, Switzerland.

APPENDIX A: EXPERIMENTAL DETAILS

High-quality single-crystals of $DyScO_3$ were obtained commercially [46]. The samples for magnetic and

specific-heat measurements were oriented using a backscattering x-ray Laue machine and then cut using a wire saw. Magnetization and AC-susceptibility measurements were performed in a temperature range 1.8–100 K, using an MPMS SQUID VSM instrument by Quantum Design. For the magnetic measurements we used a sample with mass of 1.4 mg. The sample was fixed on a quartz paddle using GE varnish. The DC magnetization data were collected using VSM technique at sample vibration frequency of 14.1 Hz. Magnetic field was applied along the [010] direction, which is the easy axis of magnetization. The specific heat measurements were carried out by the relaxation time method using a Quantum Design PPMS. The sample was attached to the platform using Apiezon-N. Contribution of the Apiezon-N was measured separately and subtracted from the data. The single crystal neutron scattering measurements used for extraction of the correlation length were done at the Cold Neutron Chopper Spectrometer (CNCS) [47,48]. To quantify the correlation lengths ξ_H, ξ_L we perform a two dimensional fitting of the (0 0 1) magnetic peak using the following function [28]:

$$S_{\mathrm{mag}}(\mathbf{Q}) = \frac{\sinh a/\xi_H}{(\cosh a/\xi_H - \cos \pi q_H)} \frac{\sinh c/\xi_L}{(\cosh c/\xi_L - \cos \pi q_L)}, \tag{A1}$$

where a and c are the lattice parameters. The calculated magnetic structure factor (see Appendix B 3) was fitted using the same equation.

To verify that $DyScO_3$ orders into commensurate AFM structure with $\mathbf{k} = (0\,0\,1)$ we performed high-resolution neutron diffraction measurements using TASP triple-axis instrument. The data were taken with $k_{\mathrm{i}} = k_{\mathrm{f}} = 1.4\,\text{Å}^{-1}$ and to improve $\mathbf{Q}$ resolution we installed 40′ and 20′ collimators between the monochromator and the sample, and the sample and the analyser, respectively.

Magnetization shows very slow dynamics below T_{N} and we measured it using following protocol: (i) ZFC to the base temperature $T = 1.8$ K; (ii) apply 100 Oe external field; (iii) wait for 3000 s; (iv) decrease the external field to zero with sweep rate of 700 Oe/s; (v) collect time-dependent $M(t)$ for 3 hours; (vi) increase temperature to the new target T and repeat from the step (ii). When choosing the protocol we consider the following reasons: (1) $DyScO_3$ exhibits a metamagnetic transition at 0.4 T and our primary target was to characterize magnetic dynamics of the zero-field AFM phase, therefore the target field should be <0.4 T. Moreover, $DyScO_3$ shows strong magnetocalloric effect and therefore we decreased the target field, so that it does not change temperature of the sample. (2) The waiting time at the target field of 100 Oe was chosen so that magnetization saturates for at least 95% of saturation at this field. Representative time dependencies of magnetization and magnetic field, which displays our protocol are shown in Fig. 10.

It was not possible to reproduce the character of low temperature relaxation data with relatively simple models like double exponent or single stretched exponent. Therefore here we made use of the inverse Laplace transform (ILT) analysis as it is occasionally done, for instance, for analysis of NMR and NQR data [49,50]. The formulation of ILT problem can

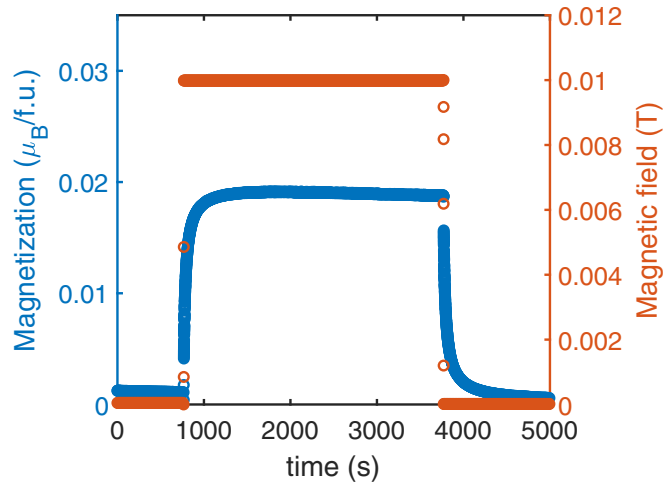

FIG. 10. Protocol used for magnetization relaxation measurements. Orange and blue points show time dependence of magnetic field and magnetization collected at $T = 1.8$ K.

be written as follows:

$$F(t) = \int_0^\infty f(z) e^{-(tz)} dz. \tag{A2}$$

The $F(t)$ is the function we want to invert, our measured data, $f(z)$ is the inverse Laplace transform and the $z = 1/\tau$ is inverse relaxation time. The $f(z)$ related to the relaxation time distribution as $zf(z) = \tau P(\tau)$. But the problem of the ILT is ill-posed and hence it has no unique solution. In case of numerical calculation of the ILT, it is a good approach to make use of the non-negativity of relaxation times and introduce some regularization parameters to decrease effect of data noise and discreetness. In this work, we used the regularized non-negative least-square method [51,52], which can be used not only for the ILT problem but also for any other inverse problems expressible in terms of linear equations. The method rewrite the ILT problem as the problem of the least squares problem:

$$\min[||\mathbf{A} - \mathbf{C}x||^2 + \alpha^2 ||\mathbf{r} - \mathbf{R}x||^2]. \tag{A3}$$

The vector $\mathbf{A}$ represents measured data, the relaxation time distribution values are contained inside the vector x and the matrix $\mathbf{C}$, which elements are exponential coefficients $e^{-(tz)}$, is ill-conditioned. The second term is the regularization part with α describing a significance of the regularization. The form of regularization term can be chosen differently and depends on particular problem, here the form enhancing solution smoothness was used:

$$||\mathbf{r} - \mathbf{R}x||^2 = \int_{z_{\min}}^{z_{\max}} (f''(z))^2 dz. \tag{A4}$$

The regularizator leads the x vector toward a smoother solution when α is increased. The noise in measured data can overtake the minimization process if α is too small, and smoothness of the solution can be overestimated if α is too high. A reasonable value of α depends on the noise level and on the sampling of original data. After the construction of the least-square problem, it is needed to solve it for the condition $x > 0$. For this purpose, the method uses Least Distance Programming algorithm [53].

APPENDIX B: MONTE CARLO SIMULATIONS

1. Magnetic Hamiltonian

At low temperature magnetic system of Dy^{3+} ions can be effectively described by dipole-dipole interaction. Since the magnetic properties of $DyScO_3$ exhibit Ising-like behavior, it is convenient to theoretically study these with Monte Carlo (MC) simulations. In this work we performed MC simulations of a 3D Ising system of Dy^{3+} moments using the classical Metropolis single-flip algorithm [37]. The Hamiltonian used in the calculations was taken as a combination of dipole-dipole interaction energy and a Zeeman term due to the external field. The Hamiltonian reads

$$\mathcal{H} = -\frac{1}{2}\frac{\mu_0}{4\pi}\sum_{i,j}\left[\frac{3(\vec{m}_i, \vec{r_{i,j}})(\vec{m}_j, \vec{r_{i,j}})}{|\vec{r_{i,j}}|^5} - \frac{(\vec{m}_i, \vec{m}_j)}{|\vec{r_{i,j}}|^3}\right] - B\sum_i \vec{m}_i\,, \tag{B1}$$

where the first term is the dipole-dipole interaction energy and the second one is the energy of Zeeman interaction of the magnetic moments and external field. Because the summation goes over each interaction twofold there is the $1/2$ factor in front of the first term. The μ_0 corresponds to vacuum permeability constant, $\vec{m}_i$ is the magnetic moment on the i site, $\vec{r_{i,j}}$ is the radius vector between the i site and j site magnetic moments, the B is the external field. In the calculations the magnitude of magnetic moments was taken as $10\mu_B$.

The crystal structure of the $DyScO_3$ was taken into account during the simulations by implementing the 3D Ising system with inter-atomic distances corresponding to the crystallographic data. This is necessary because inter-atomic radius vectors appear in the expression for the dipolar energy. The size of the system in the simulations was $10\times10\times10$ unit cells each containing 4 spins (4000 spins in total). The dipole-dipole interaction was calculated for up 62 interactions per one site (the cutoff distance between neighbours was 9.5 Å) as a compromise between calculation time and accuracy. A test simulation showed that an inclusion of further neighbors produced minor effects on the magnetic behavior. The periodic boundary conditions were used. Each Ising spin can be in the $s = 1$ or $s = -1$ state corresponding to the spin vector $\vec{S} = s(\pm\sin(\phi), \cos(\phi), 0)$, where the sign in front of the sin term depends on the position of site in unit cell (see Fig. 1). ϕ is the angle between spin vector and the [010] or the $[0\bar{1}0]$ direction determined by CEF and is equal to 28° [28].

2. AC susceptibility

AC susceptibility data were used in our simulations to adjust the time-scale transformation coefficient. For calculations of real and imaginary parts of AC susceptibility the following expressions were used:

$$\chi'(f) = \frac{1}{B_0 N_{\text{total}}}\sum_{i=0}^{N_{\text{total}}} M_i \sin\left(2\pi f\frac{i}{A} - \frac{\pi}{2}\right), \tag{B2}$$

$$\chi''(f) = \frac{1}{B_0 N_{\text{total}}}\sum_{i=0}^{N_{\text{total}}} M_i \cos\left(2\pi f\frac{i}{A} - \frac{\pi}{2}\right), \tag{B3}$$

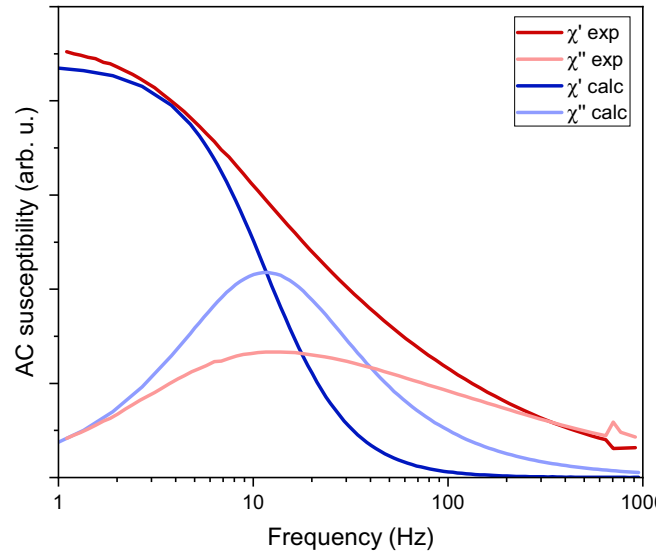

FIG. 11. Calculated and experimental AC susceptibility at $T = 4$ K.

where χ' and χ'' are real and imaginary parts of AC susceptibility, B_0 and f are the magnitude and the frequency of the alternating external field, and M_i is the magnetization of the system at ith MC step. The alternating external field at the ith MC step is taken as $B = B_0\sin(2\pi f i/A - \pi/2)$. Used external field amplitude B_0 is $0.1\,T$. The A parameter is the conversion factor between real time and simulation time $t_{\text{sim}} = At_{\text{real}}$. In the above expressions, an averaging was performed over numerous periods, with N_{total} up to 10^6 MC steps per spin. In Fig. 11, experimental and calculated AC susceptibility at temperature 4 K were drawn on the same layer for comparison. The calculated imaginary part of susceptibility χ'' consists of one symmetrical peak associated with a particular relaxation time. In contrast, the experimental dependence of χ'' is more broad and asymmetric. As it was discussed in Sec. II A, the shape of experimental χ'' curves can be interpreted as a presence of more then one relaxation channel. The value of the A parameter was adjusted for fitting the calculated position of χ'' maximum to the experimental value and later the A parameter was fixed when used in further calculations.

3. Magnetic diffraction

The magnetic structure factor was calculated as a spatial Fourier transform of the spin-spin correlation function taking into account the polarization factor of neutron scattering using the following expression:

$$S_{\text{mag}}(\vec{q}) = \sum_{\alpha,\beta}\left[\left\{\delta_{\alpha,\beta} - \frac{q_\alpha q_\beta}{|\vec{q}|^2}\right\} \times \sum_{j,j'} S_{j,\alpha}S_{j',\beta}\exp(i\vec{q}(\vec{R}_j - \vec{R}_{j'}))\right], \tag{B4}$$

where $\vec{q}$ is the wave vector, α and β are Cartesian components: x, y and z, the j and j' are the variables which go over all the sites in system, the $S_{j,\alpha}$ is the α component of spin vector

on jth site. The term in front of the second summation is the polarization factor. The isotropic magnetic form factor of Dy ions, which gives a monotonic suppression of the intensity at large Q, was not included to the calculations.

4. Thermodynamic properties

In order to achieve a better agreement with experimental measurements the magnetocaloric effect was taken into account for calculations of the field dependence of magnetization. The heat capacity used in the magnetocaloric calculations was the combination of the lattice contribution, which was obtained from approximation of experimental measurements, and the magnetic contribution which was calculated from energy fluctuations:

$$C_{\mathrm{mag}}(T,B) = \frac{\langle \mathcal{H}^2\rangle - \langle \mathcal{H}\rangle^2}{k_B T^2}, \tag{B5}$$

where k_B is the Boltzmann constant and the angle brackets means averaging over numerous MC steps. The total heat capacity can be written as $C_p = C_{\mathrm{mag}} + C_{\mathrm{lat}}$, the lattice part was approximated from experimental data above ordering temperature T_{N}. The magnetocaloric effect was implemented in calculations of the field dependence of magnetization as a variable system temperature. The temperature change comes form the magnetocaloric effect itself and also from thermal contact with the temperature reservoir. If the external field changes from B_1 to B_2 during time Δt the system temperature change ΔT can be written as follows:

$$\Delta T = \frac{T}{\frac{1}{2}(C_p(B_1,T)+C_p(B_2,T))}\frac{1}{2}\left[\frac{\partial M(B_1,T)}{\partial T} + \frac{\partial M(B_2,T)}{\partial T}\right]dB - \frac{T-T_{\mathrm{res}}}{\frac{1}{2}(C_p(B_1,T)+C_p(B_2,T))} \times \frac{1}{2}(\lambda(B_1,T)+\lambda(B_2,T))\Delta t, \tag{B6}$$

where the first term is the magnetocalorics and the second expresses thermal contact with reservoir. $dB = B_2 - B_1$ is the change of external field, T is the system temperature before the correction, T_{res} is the reservoir temperature, $\lambda(B,T)$ is the thermal conductivity coefficient. The field change dB is assumed to be small enough in order to justify the replacement of the integral from original thermodynamic formula by this simple expression. The heat capacity $C_p(B,T)$ values were obtained as it was mentioned above. The time Δt was recalculated into Monte Carlo steps with help of previously discussed

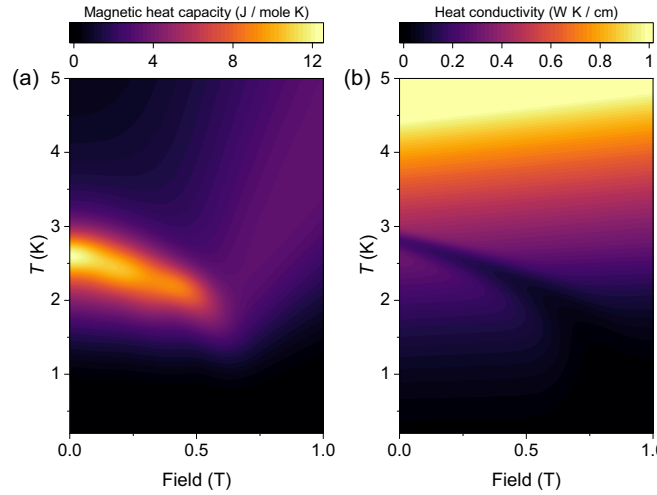

FIG. 12. (a) Calculated magnetic part of the heat capacity as function of external field and temperature. (b) The heat conductivity extrapolated in nonzero external field region.

A parameter. The partial derivative $\frac{\partial M(B,T)}{\partial T}$ was calculated beforehand from equilibrium values of magnetization:

$$\frac{\partial M(B,T)}{\partial T} = \frac{\langle M(B,T+\Delta T)\rangle - \langle M(B,T-\Delta T)\rangle}{2\Delta T}. \tag{B7}$$

In order to numerically estimate the derivative the averaging was done over more 10^6 MC steps per spin.

The exact shape of the field dependence of thermodynamic properties can significantly affect the magnetization behavior in magnetocaloric calculations. Since the experimental data for the heat conductivity $\lambda(B,T)$ is unknown in presence of external field and in low temperature for $DyScO_3$, we had to use values obtained from extrapolation process and turn into account assumptions. The heat conductivity $\lambda(B,T)$ values in zero field were taken from data for the isostructural $DyAlO_3$ material. We assumed the following when extrapolating the values to nonzero field: (i) the heat conductivity $\lambda(B,T)$ slowly decreases in the external field [38], and (ii) near the region of metamagnetic transition the heat conductivity $\lambda(B,T)$ has a pronounced drop, which often occur in AFM systems [39–41]. The points of critical field at which the heat conductivity $\lambda(B,T)$ drops were determined from anomaly on the calculated heat capacity. The heat capacity $C_p(B,T)$ and the heat conductivity $\lambda(B,T)$ as functions of external field and temperature, as these were used in our calculations, can be seen in Fig. 12.

[1] J. A. de Jong, A. V. Kimel, R. V. Pisarev, A. Kirilyuk, and T. Rasing, Laser-induced ultrafast spin dynamics in $ErFeO_3$, Phys. Rev. B **84**, 104421 (2011).

[2] K. Neeraj, N. Awari, S. Kovalev, D. Polley, N. Zhou Hagström, S. S. P. K. Arekapudi, A. Semisalova, K. Lenz, B. Green, J.-C. Deinert, I. Ilyakov, M. Chen, M. Bawatna, V. Scalera, M. d'Aquino, C. Serpico, O. Hellwig, J.-E. Wegrowe, M. Gensch, and S. Bonetti, Inertial spin dynamics in ferromagnets, Nat. Phys. **17**, 245 (2021).

[3] A. de la Torre, D. M. Kennes, M. Claassen, S. Gerber, J. W. McIver, and M. A. Sentef, Colloquium: Nonthermal pathways to ultrafast control in quantum materials, Rev. Mod. Phys. **93**, 041002 (2021).

[4] D. Gatteschi and R. Sessoli, Quantum tunneling of magnetization and related phenomena in molecular materials, Angew. Chem. Int. Ed. **42**, 268 (2003).

[5] S. K. Langley, D. P. Wielechowski, V. Vieru, N. F. Chilton, B. Moubaraki, L. F. Chibotaru, and K. S. Murray,

Modulation of slow magnetic relaxation by tuning magnetic exchange in Cr_2Dy_2 single molecule magnets, Chem. Sci. **5**, 3246 (2014).

[6] Y.-N. Guo, G.-F. Xu, Y. Guo, and J. Tang, Relaxation dynamics of dysprosium (iii) single molecule magnets, Dalton Trans. **40**, 9953 (2011).

[7] K. Matsuhira, Y. Hinatsu, and T. Sakakibara, Novel dynamical magnetic properties in the spin ice compound $Dy_2Ti_2O_7$, J. Phys.: Condens. Matter **13**, L737 (2001).

[8] J. Snyder, B. G. Ueland, J. S. Slusky, H. Karunadasa, R. J. Cava, and P. Schiffer, Low-temperature spin freezing in the $Dy_2Ti_2O_7$ spin ice, Phys. Rev. B **69**, 064414 (2004).

[9] K. Matsuhira, C. Paulsen, E. Lhotel, C. Sekine, Z. Hiroi, and S. Takagi, Spin dynamics at very low temperature in spin ice $Dy_2Ti_2O_7$, J. Phys. Soc. Jpn. **80**, 123711 (2011).

[10] H. Takatsu, K. Goto, H. Otsuka, R. Higashinaka, K. Matsubayashi, Y. Uwatoko, and H. Kadowaki, AC susceptibility of the dipolar spin ice $Dy_2Ti_2O_7$: Experiments and Monte Carlo simulations, J. Phys. Soc. Jpn. **82**, 104710 (2013).

[11] J. Gardner, G. Ehlers, P. Fouquet, B. Farago, and J. R. Stewart, Slow and static spin correlations in $Dy_{2+x}Ti_{2-x}O_{7-\delta}$, J. Phys.: Condens. Matter **23**, 164220 (2011).

[12] G. Ehlers, A. Cornelius, M. Orendac, M. Kajnakova, T. Fennell, S. Bramwell, and J. Gardner, Dynamical crossover in 'hot' spin ice, J. Phys.: Condens. Matter **15**, L9 (2003).

[13] V. Hardy, D. Flahaut, M. R. Lees, and O. A. Petrenko, Magnetic quantum tunneling in $Ca_3Co_2O_6$ studied by AC susceptibility: Temperature and magnetic-field dependence of the spin-relaxation time, Phys. Rev. B **70**, 214439 (2004).

[14] N. G. Hegde, I. Levatić, A. Magrez, H. M. Rønnow, and I. Živković, Magnetic dynamics across the in-field transition in $Ca_3Co_2O_6$, Phys. Rev. B **102**, 104418 (2020).

[15] D. Bitko, T. F. Rosenbaum, and G. Aeppli, Quantum Critical Behavior for a Model Magnet, Phys. Rev. Lett. **77**, 940 (1996).

[16] R. Giraud, W. Wernsdorfer, A. M. Tkachuk, D. Mailly, and B. Barbara, Nuclear Spin Driven Quantum Relaxation in $LiY_{0.998}Ho_{0.002}F_4$, Phys. Rev. Lett. **87**, 057203 (2001).

[17] S. Bertaina, B. Barbara, R. Giraud, B. Z. Malkin, M. V. Vanuynin, A. I. Pominov, A. L. Stolov, and A. M. Tkachuk, Cross-relaxation and phonon bottleneck effects on magnetization dynamics in $LiYF_4$:Ho^{3+}, Phys. Rev. B **74**, 184421 (2006).

[18] R. C. Johnson, B. Z. Malkin, J. S. Lord, S. R. Giblin, A. Amato, C. Baines, A. Lascialfari, B. Barbara, and M. J. Graf, Evolution of spin relaxation processes in $LiY_{1-x}Ho_xF_4$ studied via ac-susceptibility and muon spin relaxation, Phys. Rev. B **86**, 014427 (2012).

[19] S. Karimoto and M. Naito, Electron-doped infinite-layer thin films with T_C over 40 K grown on $DyScO_3$ substrates, Appl. Phys. Lett. **84**, 2136 (2004).

[20] M. D. Biegalski, J. H. Haeni, S. Trolier-McKinstry, D. G. Schlom, C. D. Brandle, and A. V. Graitis, Thermal expansion of the new perovskite substrates $DyScO_3$ and $GdScO_3$, J. Mater. Res. **20**, 952 (2005).

[21] M. D. Biegalski, E. Vlahos, G. Sheng, Y. L. Li, M. Bernhagen, P. Reiche, R. Uecker, S. K. Streiffer, L. Q. Chen, V. Gopalan, D. G. Schlom, and S. Trolier-McKinstry, Influence of anisotropic strain on the dielectric and ferroelectric properties of $SrTiO_3$ thin films on $DyScO_3$ substrates, Phys. Rev. B **79**, 224117 (2009).

[22] Y. Tokunaga, S. Iguchi, T. Arima, and Y. Tokura, Magnetic-Field-Induced Ferroelectric State in $DyFeO_3$, Phys. Rev. Lett. **101**, 097205 (2008).

[23] R. L. White, Work on the Magnetic and Spectroscopic Properties of the Rare-Earth Orthoferrites, J. Appl. Phys. **40**, 1061 (1969).

[24] M. Belakhovsky, M. Bogé, J. Chappert, and J. Sivardière, Low-temperature spin configurations in $ErFeO_3$ and $DyFeO_3$, Solid State Commun. **20**, 473 (1976).

[25] J. Wang, J. Liu, J. Sheng, W. Luo, F. Ye, Z. Zhao, X. Sun, S. A. Danilkin, G. Deng, and W. Bao, Simultaneous occurrence of multiferroism and short-range magnetic order in $DyFeO_3$, Phys. Rev. B **93**, 140403(R) (2016).

[26] C. Ritter, R. Vilarinho, J. A. Moreira, M. Mihalik, M. Mihalik, and S. Savvin, The magnetic structure of $DyFeO_3$ revisited: Fe spin reorientation and Dy incommensurate magnetic order, J. Phys.: Condens. Matter **34**, 265801 (2022).

[27] B. Biswas, V. F. Michel, O. S. Fjellvåg, G. Bimashofer, M. Döbeli, M. Jambor, L. Keller, E. Müller, V. Ukleev, E. V. Pomjakushina, D. Singh, U. Stuhr, C. A. F. Vaz, T. Lippert, and C. W. Schneider, Role of Dy on the magnetic properties of orthorhombic $DyFeO_3$, Phys. Rev. Matter. **6**, 074401 (2022).

[28] L. S. Wu, S. E. Nikitin, M. Frontzek, A. I. Kolesnikov, G. Ehlers, M. D. Lumsden, K. A. Shaykhutdinov, E.-J. Guo, A. T. Savici, Z. Gai, A. S. Sefat, and A. Podlesnyak, Magnetic ground state of the Ising-like antiferromagnet $DyScO_3$, Phys. Rev. B **96**, 144407 (2017).

[29] Y.-D. Wu, Y.-L. Qin, X.-H. Ma, R.-W. Li, Y.-Y. Wei, and Z.-F. Zi, Large rotating magnetocaloric effect at low magnetic fields in the Ising-like antiferromagnet $DyScO_3$ single crystal, J. Alloys Compd. **777**, 673 (2019).

[30] M. Bluschke, A. Frano, E. Schierle, M. Minola, M. Hepting, G. Christiani, G. Logvenov, E. Weschke, E. Benckiser, and B. Keimer, Transfer of Magnetic Order and Anisotropy Through Epitaxial Integration of 3d and 4f Spin Systems, Phys. Rev. Lett. **118**, 207203 (2017).

[31] S. Havriliak and S. Negami, A complex plane representation of dielectric and mechanical relaxation processes in some polymers, Polymer **8**, 161 (1967).

[32] C. Topping and S. Blundell, Ac susceptibility as a probe of low-frequency magnetic dynamics, J. Phys.: Condens. Matter **31**, 013001 (2019).

[33] P. Miskinis, The havriliak–negami susceptibility as a nonlinear and nonlocal process, Phys. Scr. **2009**, 014019 (2009).

[34] A. Lukichev, Physical meaning of the stretched exponential Kohlrausch function, Phys. Lett. A **383**, 2983 (2019).

[35] X. Ke, C. Adamo, D. G. Schlom, M. Bernhagen, R. Uecker, and P. Schiffer, Low temperature magnetism in the perovskite substrate $DyScO_3$, Appl. Phys. Lett. **94**, 152503 (2009).

[36] L. S. Wu, S. Nikitin, M. Brando, L. Vasylechko, G. Ehlers, M. Frontzek, A. T. Savici, G. Sala, A. D. Christianson, M. D. Lumsden, and A. Podlesnyak, Antiferromagnetic ordering and dipolar interactions of $YbAlO_3$, Phys. Rev. B **99**, 195117 (2019).

[37] I. Beichl and F. Sullivan, The metropolis algorithm, Comput. Sci. Eng. **2**, 65 (2000).

[38] T. Numazawa, H. Kimura, K. Shimamura, and T. Fukuda, Thermal conductivity of $RAlO_3$ (R = Dy, Er, and Ho) in liquid helium temperatures, J. Mater. Sci. **33**, 827 (1998).

[39] M. J. Metcalfe and H. M. Rosenberg, The magnetothermal resistivity of antiferromagnetic crystals at low temperatures. I. $DyPO_4$, a nearly ideal Ising system, J. Phys. C: Solid State Phys. **5**, 450 (1972).

[40] Z. Y. Zhao, X. G. Liu, Z. Z. He, X. M. Wang, C. Fan, W. P. Ke, Q. J. Li, L. M. Chen, X. Zhao, and X. F. Sun, Heat transport of the quasi-one-dimensional Ising-like antiferromagnet $BaCo_2V_2O_8$ in longitudinal and transverse fields, Phys. Rev. B **85**, 134412 (2012).

[41] G. S. Dixon, V. Benedict, and J. E. Rives, Low-temperature thermal conductivity of antiferromagnetic $MnCl_2 \cdot 4H_2O$, Phys. Rev. B **21**, 2865 (1980).

[42] M. E. Fisher and W. Selke, Infinitely Many Commensurate Phases in a Simple Ising Model, Phys. Rev. Lett. **44**, 1502 (1980).

[43] W. Selke, The ANNNI model–theoretical analysis and experimental application, Phys. Rep. **170**, 213 (1988).

[44] L. S. Wu, S. Nikitin, Z. Wang, W. Zhu, C. Batista, A. Tsvelik, A. Samarakoon, D. Tennant, M. Brando, L. Vasylechko, M. Frontzek, A. Savici, G. Sala, G. Ehlers, A. Christianson, M. Lumsden, and A. Podlesnyak, Tomonaga-Luttinger liquid behavior and spinon confinement in $YbAlO_3$, Nat. Commun. **10**, 698 (2019).

[45] S. E. Nikitin, S. Nishimoto, Y. Fan, J. Wu, L. S. Wu, A. Sukhanov, M. Brando, N. Pavlovskii, J. Xu, L. Vasylechko, R. Yu, and A. Podlesnyak, Multiple fermion scattering in the weakly coupled spin-chain compound $YbAlO_3$, Nat. Commun. **12**, 1 (2021).

[46] https://www.mtixtl.com/

[47] G. Ehlers, A. Podlesnyak, J. L. Niedziela, E. B. Iverson, and P. E. Sokol, The new cold neutron chopper spectrometer at the Spallation Neutron Source: design and performance, Rev. Sci. Instrum. **82**, 085108 (2011).

[48] G. Ehlers, A. Podlesnyak, and A. I. Kolesnikov, The cold neutron chopper spectrometer at the Spallation Neutron Source - A review of the first 8 years of operation, Rev. Sci. Instrum. **87**, 093902 (2016).

[49] S. K. Takahashi, J. Wang, A. Arsenault, T. Imai, M. Abramchuk, F. Tafti, and P. M. Singer, Spin Excitations of a Proximate Kitaev Quantum Spin Liquid Realized in Cu_2IrO_3, Phys. Rev. X **9**, 031047 (2019).

[50] A. Arsenault, T. Imai, P. M. Singer, K. M. Suzuki, and M. Fujita, agnetic inhomogeneity in charge-ordered $La_{1.885}Sr_{0.115}CuO_4$ studied by NMR, Phys. Rev. B **101**, 184505 (2020).

[51] S. W. Provencher, A constrained regularization method for inverting data represented by linear algebraic or integral equations, Comput. Phys. Commun. **27**, 213 (1982).

[52] https://github.com/caizkun/pyilt

[53] C. L. Lawson and R. J. Hanson, *Solving Least Squares Problems* (Society for Industrial and Applied Mathematics, Philadelphia, PA, 1995).